SCIENCE CHINA
Physics, Mechanics & Astronomy

•Article•

July 2023 Vol. 66 No. 7: 277311
https://doi.org/10.1007/s11433-022-2096-x

Electronic origin of the unusual thermal properties of copper-based semiconductors: The s-d coupling-induced large phonon anharmonicity

Kaike Yang[1,2], Huai Yang[1,3], Yujia Sun[1,3], Zhongming Wei[1,3], Jun Zhang[1,3], Ping-Heng Tan[1,3], Jun-Wei Luo[1,3*], Shu-Shen Li[1,3], Su-Huai Wei[4*], and Hui-Xiong Deng[1,3*]

[1]*State Key Laboratory of Superlattices and Microstructures, Institute of Semiconductors, Chinese Academy of Sciences, Beijing 100083, China;*
[2]*Key Laboratory of Low-Dimensional Quantum Structures and Quantum Control of Ministry of Education, Key Laboratory for Matter Microstructure and Function of Hunan Province, Synergetic Innovation Center for Quantum Effects and Applications, Department of Physics, Hunan Normal University, Changsha 410081, China;*
[3]*Center of Materials Science and Optoelectronics Engineering, University of Chinese Academy of Sciences, Beijing 100049, China;*
[4]*Beijing Computational Science Research Center, Beijing 100193, China*

Received December 7, 2022; accepted March 9, 2023; published online May 30, 2023

Copper (Cu)-based materials (such as cuprates, Cu chalcogenides, and Cu halides) often exhibit unusual properties such as superconductivity, ultralow thermal conductivity, and superionicity. However, the electronic origin of these unusual behaviors remains elusive. In this study, we demonstrate that the high-lying occupied 3d orbital of Cu causes a strong s-d coupling with its unoccupied 4s state when local symmetry is reduced. This leads to strong phonon anharmonicity and is responsible for these intriguing properties. For example, during thermal transport, symmetry-controlled s-d coupling can substantially lower the lattice potential barrier, thereby enhancing the anharmonicity and scattering between phonons and ultimately significantly reducing lattice thermal conductivity. We confirmed this understanding with Raman spectra measurements, which demonstrated a remarkable red shift in the phonon vibrational frequency with an increase in the temperature of Cu-based semiconductors. Our study shows that the cause of phonon anharmonicity is related to the fundamental electronic structures, which can also explain other unusual physical properties of the Cu compounds.

anharmonicity, copper-based semiconductor, electronic structure, thermal conductivity

PACS number(s): 65.40.-b, 71.20.Nr, 71.22.+i, 63.20.-e

Citation: K. Yang, H. Yang, Y. Sun, Z. Wei, J. Zhang, P.-H. Tan, J.-W. Luo, S.-S. Li, S.-H. Wei, and H.-X. Deng, Electronic origin of the unusual thermal properties of copper-based semiconductors: The s-d coupling-induced large phonon anharmonicity, Sci. China-Phys. Mech. Astron. **66**, 277311 (2023), https://doi.org/10.1007/s11433-022-2096-x

1 Introduction

Copper (Cu)-based materials have certain unusual physical properties such as superconductivity [1-3], superionicity [4,5], ferroelectricity [6,7], ultralow thermal conductivity [8-10], and outstanding thermoelectricity [11-16], which are extremely important in condensed matter physics and technical applications. For example, Cu atoms in Cu halides are easily off-center, which leads to a dielectric anomaly and persistent photocapacitance quenching [17]. Furthermore, in cuprate high-temperature superconductors or ferroelectrics,

*Corresponding authors (Jun-Wei Luo, email: jwluo@semi.ac.cn; Su-Huai Wei, email: suhuaiwei@csrc.ac.cn; Hui-Xiong Deng, email: hxdeng@semi.ac.cn)

the Cu-O plane has been shown to play a critical role in the transition temperatures, and this is related to the softening of phonon modes [18-22]. Furthermore, Cu atoms move unusually fast in semiconductors [23], and a high liquid-like Cu ionic motion has been observed in certain Cu-based materials, such as Cu chalcogenides [11-13].

Cu-based semiconductors are broadly used as highly efficient thermoelectric materials because they have unusually low intrinsic thermal conductivity. In this respect, Liu et al. [11-13] reported through experiments that Cu chalcogenides possess extremely low thermal conductivity of $<1\ \mathrm{W\,m^{-1}\,K^{-1}}$ at room temperature. It is known that the lattice thermal conductivities of Cu_2S, Cu_2Se, CuCl, CuBr, $CuBiS_2$, and $CuMX_2$ (M=Sb, Cr, and X=S, Se) [8-16,24,25] are approximately two orders of magnitude smaller than the adjacent Cu-free compounds such as GaP, GaAs, ZnS, ZnSe, and NaCl [26,27] and one order smaller than the leading thermoelectric material of PbTe [28,29].

Despite the many intriguing physical properties of Cu-containing materials with wide technical applications, the underlying physics and mechanism resulting in such unusual behaviors remain ambiguous. It is known that most of the intriguing physical properties of Cu-based materials are associated with their strong anharmonic effect. Furthermore, compared to non-Cu-containing materials, Cu-based materials have a unique electronic structure, which is evidently associated with Cu [17,23,30,31]. Moreover, Cu has a high-lying occupied 3d orbital, which is very close to its own 4s state in energy, as shown in Figure 1(a).

In this study, we revealed how symmetry-controlled s-d electronic state coupling can induce giant phonon anharmonicity in Cu-based semiconductors. We found that relative to other elements, the highest fully occupied 3d orbitals of Cu yielded extremely large coupling with the lowest conduction band and the s orbital when atoms vibrated under heating, which substantially lowered the lattice vibrational potential barrier, as shown in Figure 1(b). This results in the easy movement of Cu atoms (liquid-like vibration) and strong phonon anharmonicity in Cu-based materials. Our first-principles calculations were confirmed by Raman spectra measurements. This study provides an understanding of the many unusual physical properties of Cu-based compounds.

2 Theoretical and computational descriptions

We employed first-principles density functional theory combined with the Boltzmann transport approach to investigate the crystal thermal properties [32,33]. The lattice thermal conductivity of a material within the relaxation time approximation can be expressed as follows [34-36]:

$$\kappa = \frac{1}{N_{\mathbf{q}}\Omega}\sum_{\mathbf{q}\nu}\mathbf{v}_{\mathbf{q}\nu}\otimes\mathbf{v}_{\mathbf{q}\nu}c_{\mathbf{q}\nu}\tau_{\mathbf{q}\nu}, \tag{1}$$

where $N_{\mathbf{q}}$ is the number of sampling $\mathbf{q}$ points in the Brillouin zone, Ω the volume of the unit cell of investigated materials, $\mathbf{v}_{\mathbf{q}\nu}$ is the group velocity of phonons with wave-vector $\mathbf{q}$ and branch ν, and $c_{\mathbf{q}\nu}$ is the heat capacity. The mode-dependent phonon scattering rate takes the form of [36]

$$\begin{aligned}\gamma_{\mathbf{q}\nu}(\omega) = \frac{1}{2\tau_{\mathbf{q}\nu}(\omega)} = \frac{18\pi}{\hbar^2}\sum_{\mathbf{q}'\nu'}\sum_{\mathbf{q}''\nu''}\left|\mathbf{V}^{(3)}_{\mathbf{q}\nu,\mathbf{q}'\nu',\mathbf{q}''\nu''}\right|^2 \\ \times[(n_{\mathbf{q}'\nu'}+n_{\mathbf{q}''\nu''}+1)\,\delta(\omega-\omega_{\mathbf{q}'\nu'}-\omega_{\mathbf{q}''\nu''}) \\ +(n_{\mathbf{q}'\nu'}-n_{\mathbf{q}''\nu''})\delta(\omega+\omega_{\mathbf{q}'\nu'}-\omega_{\mathbf{q}''\nu''}) \\ +(n_{\mathbf{q}''\nu''}-n_{\mathbf{q}'\nu'})\delta(\omega+\omega_{\mathbf{q}''\nu''}-\omega_{\mathbf{q}'\nu'})] \\ \times\delta(\mathbf{q}+\mathbf{q}'+\mathbf{q}''-\mathbf{G}),\end{aligned} \tag{2}$$

where $\tau_{\mathbf{q}\nu}$ is the phonon lifetime, $\hbar$ is the reduced Planck constant, $\mathbf{V}^{(3)}_{\mathbf{q}\nu,\mathbf{q}'\nu',\mathbf{q}''\nu''}$ are the third-order anharmonic matrix

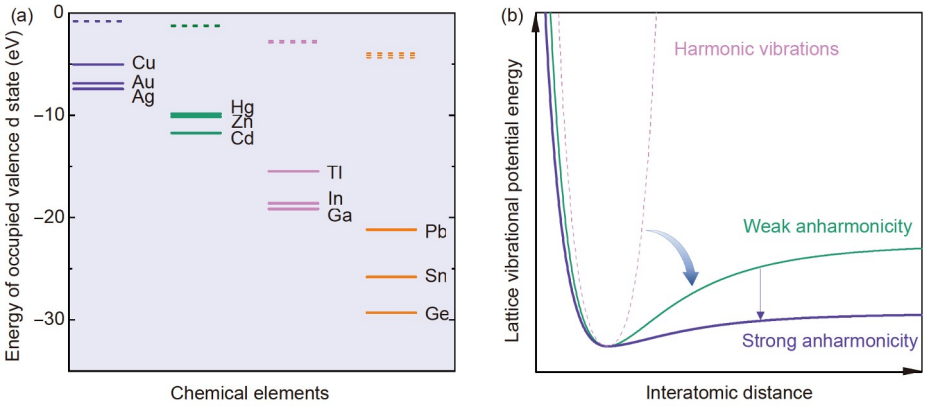

Figure 1 (Color online) (a) Chemical trend of fully occupied valence *n*d orbital energy levels (solid lines) and the corresponding (*n*+1)s state energy levels (dashed lines) of atoms; this shows that Cu (*n*=3) has the highest occupied *n*d orbital energy level and the smallest energy separation between its *n*d and (*n*+1)s energy levels among the elements. (b) Schematic of lattice vibrational potential energy as a function of interatomic distance, where the dashed line indicates harmonic oscillation and cyan and violet curves represent anharmonic vibrations. The strength of the anharmonicity is quantified by the deviation of potential energy from the harmonic vibration.

elements where the summation includes all allowable scattering processes in which a phonon with wave-vector $\mathbf{q}$ decays into two phonons ($\mathbf{q}'\nu'$) and ($\mathbf{q}''\nu''$), or in which a phonon with wave-vector $\mathbf{q}$ initially coalesces with ($\pm\mathbf{q}'\nu'$) and then emits ($\mp\mathbf{q}''\nu''$), while the energy and momentum conservation of the scattering processes is guaranteed by the Dirac functions. The normal and umklapp scattering processes can be identified as per $\mathbf{q}'$ and $\mathbf{q}''$ when $\mathbf{q}+\mathbf{q}'+\mathbf{q}''=\mathbf{0}$ or $\mathbf{G}$, where $\mathbf{G}$ is the reciprocal lattice vector, respectively. For convenience, we define an averaged scattering rate as follows:

$$\gamma(\omega)=\frac{1}{N_\nu N_{\mathbf{q}}}\sum_{\mathbf{q}\nu}\gamma_{\mathbf{q}\nu}(\omega), \tag{3}$$

where N_ν is the total number of acoustic and optical phonon branches.

To calculate the frequency shifts because of the phonon anharmonic effect, we employed first-principles density functional perturbation theory [37], and the temperature-dependent lattice vibrational frequency was obtained by $\omega_{\mathbf{q}\nu}(T)=\omega_{\mathbf{q}\nu}(0)+\Delta\omega_{\mathbf{q}\nu}$ [38], where

$$\Delta\omega_{\mathbf{q}\nu}=\mathrm{Re}\left\{\frac{1}{\hbar}\sum_{\mathbf{q}'\nu'}\sum_{\mathbf{q}''\nu''}\left|\mathbf{V}^{(3)}_{\mathbf{q}\nu,\mathbf{q}'\nu',\mathbf{q}''\nu''}\right|^2\delta(\mathbf{q}+\mathbf{q}'+\mathbf{q}''-\mathbf{G})\times\right.$$
$$\left.\left[\frac{(\omega_{\mathbf{q}'\nu'}+\omega_{\mathbf{q}''\nu''})(n_{\mathbf{q}'\nu'}+n_{\mathbf{q}''\nu''}+1)}{(\omega+\mathrm{i}\eta)^2-(\omega_{\mathbf{q}'\nu'}+\omega_{\mathbf{q}''\nu''})^2}+\frac{(\omega_{\mathbf{q}'\nu'}-\omega_{\mathbf{q}''\nu''})(n_{\mathbf{q}''\nu''}-n_{\mathbf{q}'\nu'})}{(\omega+\mathrm{i}\eta)^2-(\omega_{\mathbf{q}'\nu'}-\omega_{\mathbf{q}''\nu''})^2}\right]\right\}, \tag{4}$$

in which $\omega_{\mathbf{q}\nu}(0)$ is the lattice vibrational frequency at harmonic oscillations, η is a small positive quantity added to avoid divergence in practical computations, and $n_{\mathbf{q}'\nu'}$ or $n_{\mathbf{q}''\nu''}$ are the Bose-Einstein distribution functions.

Before calculating the electronic structures and lattice dynamical properties of a material, we first relaxed the lattice constants and the atomic positions in the unit cell by performing the first-principles density functional theory calculations as implemented in the Vienna *Ab initio* Simulation Package [32,33]. For this purpose, we used the projector augmented wave method [39,40] and the generalized gradient approximation, which was parametrized in the form of Perdew-Burke-Ernzerhof [41] for exchange-correlation potentials. We sampled the k-points using a 10×10×10 Monkhorst-Pack grid [42] to ensure self-consistent calculations. The kinetic energy cut-off for the plane wave basis set was 500 eV, and the total energy threshold for convergence was 10^{-8} eV. After ionic relaxation, the Hellmann-Feynman forces acting on each atom were less than 10^{-6} eV/Å. Once we obtained the optimal atomic arrangements in the material, we used the finite displacement method to calculate the interatomic force constants (IFCs) [36]. The second-order IFCs were calculated using 6×6×6 supercells with k-points and employing a 2×2×2 Monkhorst-Pack grid, and we used 3×3×3 supercells for third-order IFCs calculations. We calculated the lattice thermal conductivity by sampling 30×30×30 integration q-point meshes based on the relaxation time approximation by using VASP and Phono3py software [34,35].

To calculate the anharmonic-induced phonon frequency shifts in solids, as shown in eq. (4), we used first-principles density functional perturbation theory as implemented in the Quantum-Espresso code [43,44]. The norm-conserving pseudopotentials for treating the valence electrons of atoms were used [39,45], and the generalized-gradient approximation, which was parametrized in the form of Perdew-Burke-Ernzerhof for exchange-correlation potentials [41]. To obtain the ground state electronic structural properties, we minimized the total energy of the materials, where the kinetic energy cut off for the plane wave basis set was selected as 120 Ry. The total energy threshold for convergence was 1×10^{-12} Ry, and the force threshold for each atom was 1×10^{-10} Ry/Bohr. We sampled the k-points in the Brillouin zone on a 24×24×24 Monkhorst-Pack mesh to ensure self-consistent field calculations [42]. After ionic relaxation and to conduct the phonon calculations, we sampled the k-points of 9×9×9 for non-self-consistent electronic structure calculations, and we set the q-points of 6×6×6 for the second-order IFCs calculations. For the third-order IFCs calculations, we sampled the q-points of the 3×3×3 meshes. Finally, the frequency shifts and line widths of different phonon modes were obtained using a 30×30×30 integration mesh.

3 The role of s-d coupling in the thermal conductivity of Cu-based semiconductors

In the following, as an example, we elucidate how s-d coupling enhances the phonon anharmonicity of Cu-based semiconductors and thus causes ultralow thermal conductivity. Zinc-blende structured CuCl was selected as the Cu-based compound. Figure 2(a) shows a comparison between the intrinsic lattice thermal conductivities of several prototypical crystalline semiconductors as a function of temperature. The $\kappa(T)$ (pink solid line) of CuCl is shown and compared with that of Si, GaAs and ZnSe, which have the same lattice structure as CuCl, and their corresponding experimental data (dots) [26,27,46-51] are shown where available. These results show that the theoretical result agrees well with the experimental data. As the temperature rises, the thermal conductivity decreases (as expected) because of the enhanced phonon scattering effect. Moving from Si and passing through GaAs and ZnSe to CuCl, the thermal conductivity monotonically decreases within the investigated temperature range. Interestingly, the Cu-based compound exhibits extremely low thermal conductivity compared with traditional semiconductor materials, no

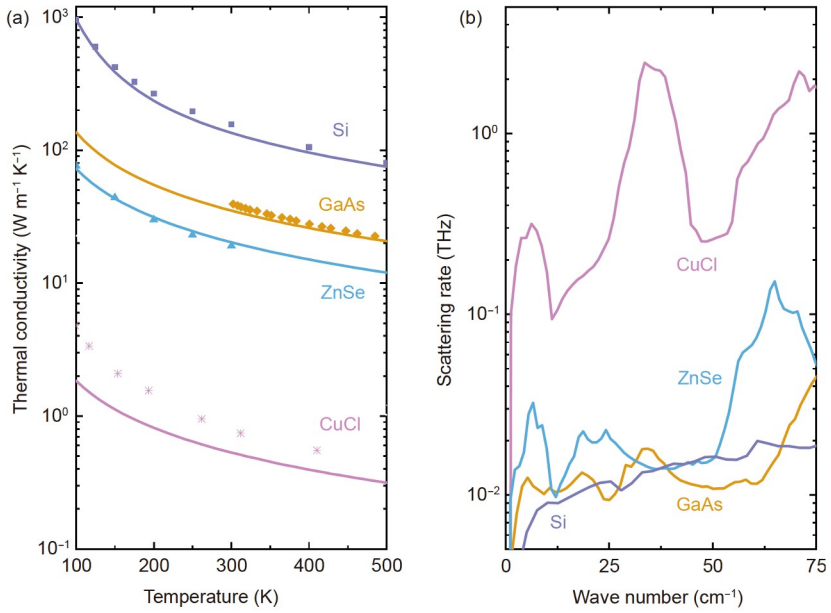

Figure 2 (Color online) Evaluation of the lattice thermal conductivity and phonon scattering effect. (a) First-principles calculated thermal conductivity κ (solid curves) as a function of temperature for CuCl, ZnSe, GaAs and Si, while all experimental data (sparse dots) are taken from refs. [26,27,46-51], when available. We use a consistent color for each material but use different symbols to distinguish between the theoretical and experimental results. (b) Average phonon scattering rate as a function of wave number for all investigated materials.

matter how light their chemical composition is. The lattice thermal conductivity of CuCl is nearly two orders of magnitude smaller than that of adjacent GaAs and ZnSe in the periodic table and three orders of magnitude smaller than Si. The phonon scattering rate that dominates thermal conductivity as a function of wave number for all investigated materials is shown in Figure 2(b), where it is evident that CuCl exhibits the largest scattering rate.

Compared with other semiconductor materials, the most prominent feature of Cu-based compounds is their high-lying occupied d orbitals in energy [17,23,30,31,52]. The atomic energy of 3d electrons in Cu is even higher than that of the outermost valence p states in chalcogen and halogen elements but extremely close to its own 4s state (Figure 1(a)). Considering the zinc-blende structure of Cu halides with T_d symmetry, the occupied d orbitals are transformed to irreducible representations of two-fold degenerate E and three-fold degenerate T_2 states, respectively, whereas, the high-lying unoccupied s orbital is transformed to A_1. There is, thus, no coupling between the occupied d orbitals and the unoccupied s orbitals because they have no common symmetry. However, thermal vibrations reduce the crystal symmetry to C_1, in which the coupling between occupied d orbitals and unoccupied s orbitals is allowed because the symmetry of both the d and s orbitals is transformed to A. Such s-d coupling pushes the occupied d orbital down in energy and lowers the total energy, which reduces the potential barrier of atomic vibrations. The strength of this allowed s-d coupling is inversely proportional to the energy separation between occupied d orbitals and unoccupied s orbitals; therefore, the enhanced anharmonicity occurs as the occupied d and unoccupied s orbital energy separation decreases, i.e., with an increase in d orbital energy.

Our expectations were confirmed by the first-principles calculations, as shown in Figure 3, where we calculated the vibrational potential energy as a function of the displacement of atoms away from their equilibrium center. For the considered materials, we displaced cations (i.e., Cu, Zn, Ga or Si) in the corresponding compounds along the bond-stretching (i.e., [111]) direction. In the inset of Figure 3, we show how s-d coupling effectively reduces the system potential energy and thus enhances the phonon anharmonicity. Moving from Cu to Zn and Ga, their occupied 3d orbital becomes deeper and deeper, and therefore the s-d coupling contributes less and less to the potential energy surface. The vibrational potential energy of GaAs and ZnSe was reported to be much higher than that of CuCl, while Si exhibited the highest potential energy of them all because of the lack of s-d coupling.

Although coupling between Cu's unoccupied 4s orbital and anion's occupied p state occurs in the Cu-based compounds because of symmetry reduction, this effect is weak because (1) the unoccupied 4s state from the cation and occupied p state from the anion are separated in space, and therefore their wavefunction overlap is small, whereas the s-d coupling in Cu occurs within the same Cu atom; (2) the energy difference between the occupied p state of the anion and unoccupied s state of the cation is usually larger than that

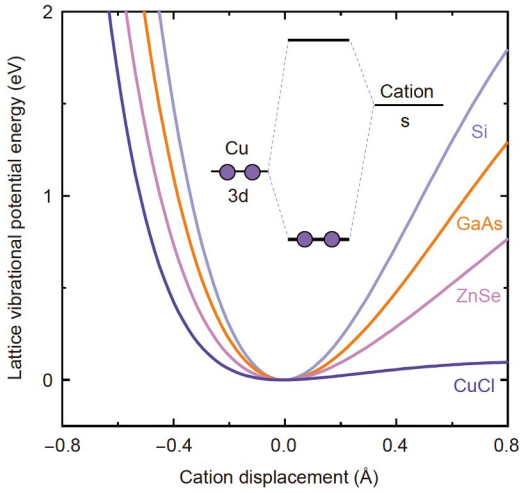

Figure 3 (Color online) First-principles calculations of the vibrational potential energy as a function of atomic displacement, where the potential energies at equilibrium were set as zero for comparison. We displaced cations of Cu, Zn, Ga, and Si along the bond-stretching (i.e., [111]) direction in Cu compounds, ZnSe, GaAs, and Si, respectively. It is evident that CuCl exhibited the lowest vibrational potential energy surface compared with the traditional semiconductors investigated at a given interatomic spacing, and the inset shows the band coupling between the 3d and 4s states of Cu schematically.

of Cu's 3d and 4s orbitals, which results in the former having a weaker coupling strength than the latter.

To further confirm our theory, we conducted advanced DFT+U calculations [53,54] and artificially adjusted the s-d coupling strength to verify the changes in the lattice thermal conductivity of Cu-based compounds, as shown in Figure 4. According to the above discussion, lattice thermal conductivity was expected to increase if the s-d coupling strength was reduced. To modulate the strength of s-d coupling in the Cu-based compounds, we added a positive Coulomb repulsive energy U on the Cu 3d orbital, which increased the energy spacing between Cu's occupied 3d and unoccupied 4s states. As shown in Figure 4(a), the lattice vibrational potential energy of CuCl increased with an increase in U. Accordingly, the scattering rate decreased (Figure 4(b)), and the thermal conductivity increased (Figure 4(c)) because of the reduced s-d coupling strength that weakened the phonon anharmonicity originating from the lowering of the Cu 3d orbital in energy and the accompanied wave function localization (Figure 4(c)).

One of the consequences of large phonon anharmonicity is phonon frequency softening at an increased temperature. We investigated the phonon frequency shift of the optical phonons of CuCl at the center of the Brillouin zone with a change in temperature, and the results are shown in Figure 4(d). For this purpose, we conducted density functional perturbation theory calculations to obtain $\Delta\omega_{qv}(T)$ $\left(\Delta\omega_{qv}(T)=\omega_{qv}(T)-\omega_{qv}(0)\right)$. In the harmonic system, the phonon frequency is independent of temperature. Therefore, when anharmonicity is stronger, $\Delta\omega_{qv}$ is larger. For GaAs, $\Delta\omega_{qv}$ was very small, but for CuCl, the phonon frequency significantly decreased with an increase in temperature. The magnitude of the reduction was reduced as the s-d coupling weakened as U increased; this again shows that the s-d coupling is the root of strong phonon anharmonicity in Cu-based materials.

The phonon velocity of CuCl, which also plays an important role in the lattice thermal conductivity, as shown in eq. (1), is low compared with other semiconductor materials because of the ionic character (weak chemical bond) of Cu-based semiconductors and the relatively large p-d coupling, which places the antibonding character at the top of the valence bands [55].

4 Experimental evidence of strong anharmonicity in Cu halides

To confirm our predictions of the large anharmonicity of Cu-based compounds, we performed temperature-dependent Raman spectra measurements using CuCl as an example. A high-quality single crystal of CuCl with a zinc-blende lattice was synthesized using the chemical vapor transport technique, and 1.9 g CuCl powder (Alfa, 99.999%) and 0.1 g KCl powder (Alfa, 99.999%) were placed in an ampoule. The KCl powder was used to lower the temperature below the phase transition point (407°C) and to avoid the formation of undesired wurtzite CuCl crystals [56]. The ampoule was evacuated to the lowest pressure attained in our lab (10^5 Torr) and immediately sealed. The synthesis was conducted in a horizontal two-zone tube furnace system, and the growth temperature gradient was set to 350°C/450°C under heating 10 h. Samples were left at a temperature difference for 10 d. The system was finally cooled down to room temperature at a 10°C/h rate. The resulting CuCl crystals were transparent with a length of several millimeters, and they were mainly concentrated in the bottle. The X-ray diffraction (XRD) pattern of the single crystal CuCl is shown in Figure 5(a). The characteristic peaks of the zinc-blende structure with a space group $F\bar{4}3m$ were evident, which confirmed the sample quality of single crystal CuCl.

We then conducted temperature-dependent Raman measurements using a p-type (100) Si wafer and a SiO_2 layer with a thickness of 300 nm as the substrate. Raman measurements were undertaken using backscattering geometry via a Jobin-Yvon HR800 system (France) equipped with a liquid-nitrogen-cooled charge-coupled detector. The Raman spectra were collected at low temperatures using a 50× long-working-distance objective lens (NA=0.5) and a grating of 1800 lines/mm. To avoid excessive laser heating on the sample, a conventional He-Cd laser with a typical laser

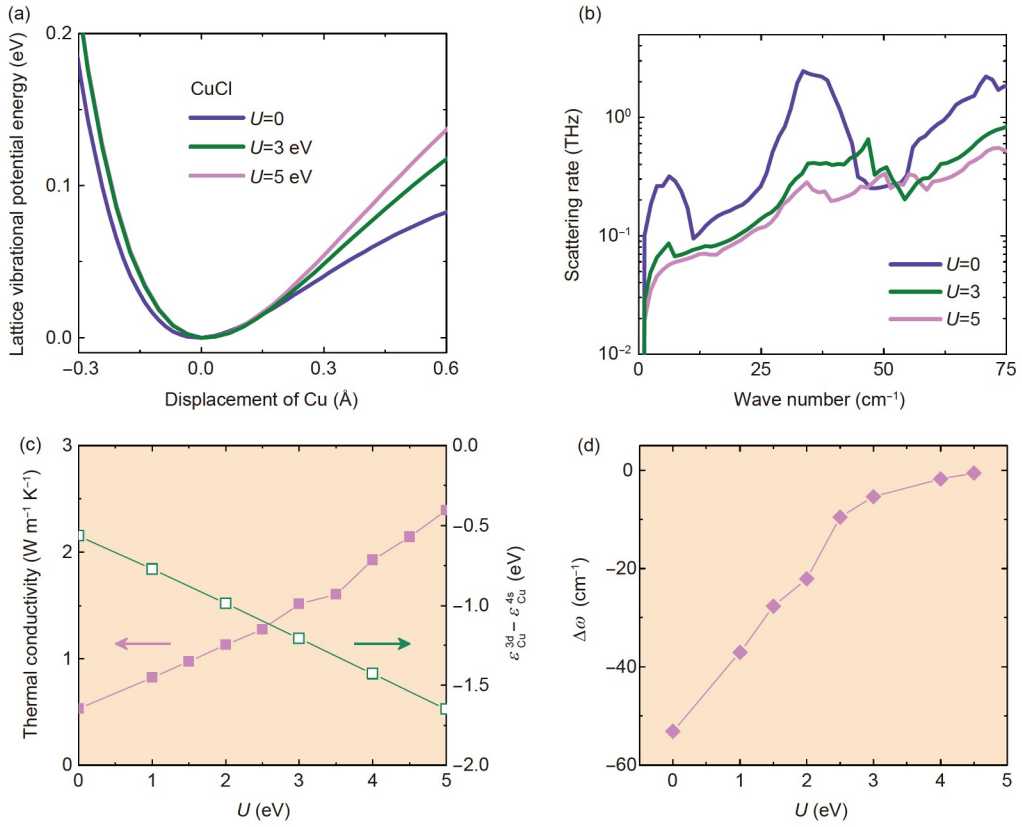

Figure 4 (Color online) Artificial modulation of s-d coupling effect in the thermal transport of Cu-based semiconductors. (a) Lattice vibrational potential energy of CuCl as a function of Cu's displacement along the bond-stretching direction under different Coulomb repulsive interactions, U, which were applied on Cu 3d orbitals. (b) Scattering rate and (c) thermal conductivity of CuCl under different U, where the corresponding energy difference between Cu's 3d and 4s states in CuCl is also presented. (d) Anharmonicity caused a frequency shift of optical phonon modes at the center of the Brillouin zone in CuCl between T=300 and 0 K.

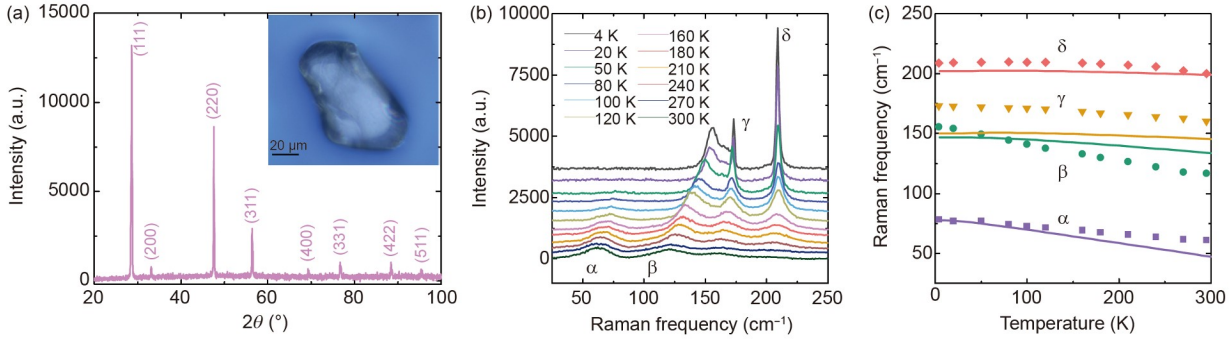

Figure 5 (Color online) Experimental evidence of anharmonicity-induced phonon mode softening in Cu-based materials. (a) Wide angle X-ray diffraction patterns were obtained with an ultima IV diffractometer equipped with Cu Kα radiation (40 kV, 40 mA) over an angle range from 20° to 100°. The XRD spectrum confirms that the CuCl crystal is a single-phase zinc-blende structure. The inset shows an optical microscopy image of a CuCl single crystal under a 100× long-working-distance objective lens. (b) Raman spectra of CuCl single crystal in a temperature range from 4 to 300 K. From low to high frequency, the α peak is contributed to by a combination of longitudinal and transverse acoustic modes, β and γ bands are mainly obtained from the transverse optic phonon modes, whereas δ band relates to the vibrations of longitudinal optic modes, respectively. (c) Measured Raman frequency shift of the four peaks labeled in (b). To verify the experimental results, we conducted first-principles calculations of the phonon frequency at a finite temperature in consideration of anharmonicity (solid lines).

power of about 0.8 mW was used to determine the excitation wavelength of zincblende cubic CuCl (442 nm). In Figure 5(b), we present the Raman vibrational spectra measured over a wide temperature range from 4 to 300 K. Four pronounced lattice vibrational peaks were identified and labeled using α, β, γ and δ, which correspond to the phonon energies of $\omega \approx 65$, 155, 166, and 209 cm^{-1}, respectively. Previous studies [57,58] have shown that the symmetric δ peak is

obtained from the zone-center vibrations of longitudinal optical phonon modes, whereas the α band is a combination of the longitudinal and transverse acoustic mode, and β and γ bands are attributed to the transverse optical phonon modes.

The Raman measured frequency shift of the four vibrational peaks indicated in Figure 5(b) is shown in Figure 5(c). With an increase in the temperature, all the peaks shifted to a lower frequency regime, and there was a remarkable energy reduction for α, β and γ bands. This suggests that significant phonon mode softening occurred, which confirms the giant phonon anharmonicity of Cu-based compounds. Our first-principles simulations (solid lines) were consistent with the experimental observations (dots), where the discrepancy in amplitude for γ band was likely related to the Cu atoms in CuCl that had been considerably displaced from their ideal position [59].

In addition to binary Cu compounds, it was recently found that a few ternary Cu-based materials, such as $CuBiS_2$ [9], $CuSbX_2$ [10,15] and $CuCrX_2$ (X=S or Se), exhibit very low thermal conductivity [4,5,60-63]. In particular, Niedziela et al. [4] reported through experiments that $CuCrSe_2$ has a liquid-like thermal diffusive behavior at a relatively high temperature, which is caused by breaking down the Cu ion-dominated vibrations in the low-energy regime. Applying our theory above, this behavior is understood to be related to the strong band-to-band coupling between Cu unoccupied 4s and occupied 3d states. This study, therefore, shows that Cu ions have a prominent role in the vibrational dynamics of these materials.

5 Conclusions

In summary, we conducted first-principles calculations and experimental measurements to investigate the physics and mechanisms underlying the many unusual behaviors of Cu-based materials, which are related to their strong phonon anharmonicity. We revealed that the symmetry-controlled s-d coupling between Cu's occupied 3d and unoccupied 4s orbitals flattens the lattice vibrational potential energy surface, which results in the easy movement of atoms and the strong phonon anharmonicity responsible for the intriguing properties of Cu-based materials. This study elucidates the connection between electronic structures and phonon anharmonicity, and it thus provides new insights into understanding materials properties that rely on strong electron–phonon coupling.

This work was supported by the National Natural Science Foundation of China (Grant Nos. 12174099, 61922077, 11874347, 12088101, 11991060, and U2230402), the National Key Research and Development Program of China (Grant Nos. 2018YFB2200100, and 2020YFB1506400), the Key Research Program of the Chinese Academy of Sciences (Grant No. XDPB22), and the Beijing Science and Technology Committee (Grant No. Z181100005118003). Hui-Xiong Deng was also supported by the Youth Innovation Promotion Association of the Chinese Academy of Sciences (Grant No. Y2021042).

1 F. Giustino, M. L. Cohen, and S. G. Louie, Nature **452**, 975 (2008).
2 A. Lanzara, P. V. Bogdanov, X. J. Zhou, S. A. Kellar, D. L. Feng, E. D. Lu, T. Yoshida, H. Eisaki, A. Fujimori, K. Kishio, J. I. Shimoyama, T. Noda, S. Uchida, Z. Hussain, and Z. X. Shen, Nature **412**, 510 (2001).
3 J. G. Bednorz, and K. A. Muller, Z. Physik B-Condensed Matter **64**, 189 (1986).
4 J. L. Niedziela, D. Bansal, A. F. May, J. Ding, T. Lanigan-Atkins, G. Ehlers, D. L. Abernathy, A. Said, and O. Delaire, Nat. Phys. **15**, 73 (2019).
5 R. Yakshibayev, V. N. Zabolotsky, and R. F. Almukhametov, Solid State Ion. **31**, 1 (1988).
6 Z. Viskadourakis, I. Radulov, A. P. Petrović, S. Mukherjee, B. M. Andersen, G. Jelbert, N. S. Headings, S. M. Hayden, K. Kiefer, S. Landsgesell, D. N. Argyriou, and C. Panagopoulos, Phys. Rev. B **85**, 214502 (2012).
7 K. Nakagawa, H. Tokoro, and S. Ohkoshi, Inorg. Chem. **47**, 10810 (2008).
8 S. Mukhopadhyay, D. Bansal, O. Delaire, D. Perrodin, E. Bourret-Courchesne, D. J. Singh, and L. Lindsay, Phys. Rev. B **96**, 100301 (2017).
9 Z. Feng, T. Jia, J. Zhang, Y. Wang, and Y. Zhang, Phys. Rev. B **96**, 235205 (2017).
10 B. Du, R. Zhang, K. Chen, A. Mahajan, and M. J. Reece, J. Mater. Chem. A **5**, 3249 (2017).
11 H. Liu, X. Shi, F. Xu, L. Zhang, W. Zhang, L. Chen, Q. Li, C. Uher, T. Day, and G. J. Snyder, Nat. Mater. **11**, 422 (2012).
12 D. Voneshen, H. Walker, K. Refson, and J. Goff, Phys. Rev. Lett. **118**, 145901 (2017).
13 Y. He, T. Day, T. Zhang, H. Liu, X. Shi, L. Chen, and G. J. Snyder, Adv. Mater. **26**, 3974 (2014).
14 K. S. Weldert, W. G. Zeier, T. W. Day, M. Panthöfer, G. J. Snyder, and W. Tremel, J. Am. Chem. Soc. **136**, 12035 (2014).
15 D. Zhang, J. Yang, Q. Jiang, L. Fu, Y. Xiao, Y. Luo, and Z. Zhou, J. Mater. Chem. A **4**, 4188 (2016).
16 D. Byeon, R. Sobota, K. Delime-Codrin, S. Choi, K. Hirata, M. Adachi, M. Kiyama, T. Matsuura, Y. Yamamoto, M. Matsunami, and T. Takeuchi, Nat. Commun. **10**, 72 (2019).
17 S. H. Wei, S. B. Zhang, and A. Zunger, Phys. Rev. Lett. **70**, 1639 (1993).
18 C. Setty, M. Baggioli, and A. Zaccone, Phys. Rev. B **102**, 174506 (2020).
19 R. J. McQueeney, Y. Petrov, T. Egami, M. Yethiraj, G. Shirane, and Y. Endoh, Phys. Rev. Lett. **82**, 628 (1999).
20 S. R. Park, A. Hamann, L. Pintschovius, D. Lamago, G. Khaliullin, M. Fujita, K. Yamada, G. D. Gu, J. M. Tranquada, and D. Reznik, Phys. Rev. B **84**, 214516 (2011).
21 V. H. Crespi, and M. L. Cohen, Phys. Rev. B **48**, 398 (1993).
22 A. P. Menushenkov, A. V. Kuznetsov, R. V. Chernikov, A. A. Ivanov, V. V. Sidorov, and K. V. Klementiev, J. Supercond. Nov. Magn. **27**, 925 (2014).
23 H. X. Deng, J. W. Luo, S. S. Li, and S. H. Wei, Phys. Rev. Lett. **117**, 165901 (2016).
24 D. L. Perry, *Handbook of Inorganic Compounds* (CRC Press, New York, 2011).
25 H. Kim, S. Ballikaya, H. Chi, J. P. Ahn, K. Ahn, C. Uher, and M. Kaviany, Acta Mater. **86**, 247 (2015).
26 G. A. Slack, J. Phys. Chem. Solids **34**, 321 (1973).
27 D. P. Spitzer, J. Phys. Chem. Solids **31**, 19 (1970).
28 O. Delaire, J. Ma, K. Marty, A. F. May, M. A. McGuire, M. H. Du, D. J. Singh, A. Podlesnyak, G. Ehlers, M. D. Lumsden, and B. C. Sales, Nat. Mater. **10**, 614 (2011).

29 K. Biswas, J. He, I. D. Blum, C. I. Wu, T. P. Hogan, D. N. Seidman, V. P. Dravid, and M. G. Kanatzidis, Nature **489**, 414 (2012).
30 X. Nie, S. H. Wei, and S. B. Zhang, Phys. Rev. Lett. **88**, 066405 (2002).
31 K. Yang, J. Xiao, J. W. Luo, S. S. Li, S. H. Wei, and H. X. Deng, New J. Phys. **21**, 123015 (2019).
32 R. M. Dreizler, and E. K. U. Gross, *Density Functional Theory* (Springer, New York, 1990).
33 W. Kohn, and L. J. Sham, Phys. Rev. **140**, A1133 (1965).
34 G. D. Mahan, *Many-Particle Physics* (Springer, New York, 2000).
35 J. M. Ziman, *Electrons and Phonons* (Oxford University Press, New York, 1960).
36 A. Togo, L. Chaput, and I. Tanaka, Phys. Rev. B **91**, 094306 (2015).
37 S. Baroni, S. de Gironcoli, A. Dal Corso, and P. Giannozzi, Rev. Mod. Phys. **73**, 515 (2001).
38 L. Paulatto, I. Errea, M. Calandra, and F. Mauri, Phys. Rev. B **91**, 054304 (2015).
39 G. Kresse, and J. Furthmüller, Phys. Rev. B **54**, 11169 (1996).
40 G. Kresse, and D. Joubert, Phys. Rev. B **59**, 1758 (1999).
41 J. P. Perdew, K. Burke, and M. Ernzerhof, Phys. Rev. Lett. **77**, 3865 (1996).
42 H. J. Monkhorst, and J. D. Pack, Phys. Rev. B **13**, 5188 (1976).
43 P. Giannozzi, S. Baroni, N. Bonini, M. Calandra, R. Car, C. Cavazzoni, D. Ceresoli, G. L. Chiarotti, M. Cococcioni, I. Dabo, A. Dal Corso, S. de Gironcoli, S. Fabris, G. Fratesi, R. Gebauer, U. Gerstmann, C. Gougoussis, A. Kokalj, M. Lazzeri, L. Martin-Samos, N. Marzari, F. Mauri, R. Mazzarello, S. Paolini, A. Pasquarello, L. Paulatto, C. Sbraccia, S. Scandolo, G. Sclauzero, A. P. Seitsonen, A. Smogunov, P. Umari, and R. M. Wentzcovitch, J. Phys.-Condens. Matter **21**, 395502 (2009).
44 P. Giannozzi, O. Andreussi, T. Brumme, O. Bunau, M. Buongiorno Nardelli, M. Calandra, R. Car, C. Cavazzoni, D. Ceresoli, M. Cococcioni, N. Colonna, I. Carnimeo, A. Dal Corso, S. de Gironcoli, P. Delugas, R. A. DiStasio Jr, A. Ferretti, A. Floris, G. Fratesi, G. Fugallo, R. Gebauer, U. Gerstmann, F. Giustino, T. Gorni, J. Jia, M. Kawamura, H. Y. Ko, A. Kokalj, E. Küçükbenli, M. Lazzeri, M. Marsili, N. Marzari, F. Mauri, N. L. Nguyen, H. V. Nguyen, A. Otero-de-la-Roza, L. Paulatto, S. Poncé, D. Rocca, R. Sabatini, B. Santra, M. Schlipf, A. P. Seitsonen, A. Smogunov, I. Timrov, T. Thonhauser, P. Umari, N. Vast, X. Wu, and S. Baroni, J. Phys.-Condens. Matter **29**, 465901 (2017).
45 P. E. Blöchl, Phys. Rev. B **50**, 17953 (1994).
46 G. A. Slack, and P. Andersson, Phys. Rev. B **26**, 1873 (1982).
47 E. F. Steigmeier, and I. Kudman, Phys. Rev. **141**, 767 (1966).
48 G. A. Slack, Phys. Rev. B **6**, 3791 (1972).
49 C. J. Glassbrenner, and G. A. Slack, Phys. Rev. **134**, A1058 (1964).
50 Y. Lu, T. Sun, and D. B. Zhang, Phys. Rev. B **97**, 174304 (2018).
51 B. Håkansson, and P. Andersson, J. Phys. Chem. Solids **47**, 355 (1986).
52 L. D. Yuan, H. X. Deng, S. S. Li, S. H. Wei, and J. W. Luo, Phys. Rev. B **98**, 245203 (2018).
53 J. Hubbard, Proc. R. Soc. Lond. A **276**, 238 (1963).
54 W. Gao, W. Xia, Y. Wu, W. Ren, X. Gao, and P. Zhang, Phys. Rev. B **98**, 045108 (2018).
55 S. H. Wei, and A. Zunger, Phys. Rev. B **37**, 8958 (1988).
56 Y. Kaifu, Y. Kawate, S. Nakanishi, I. Niwa, K. Nakazawa, and M. Koba, J. Phys. Soc. Jpn. **22**, 517 (1967).
57 J. E. Potts, R. C. Hanson, C. T. Walker, and C. Schwab, Phys. Rev. B **9**, 2711 (1974).
58 T. Fukumoto, K. Tabuchi, S. Nakashima, and A. Mitsuishi, J. Phys. Soc. Jpn. **35**, 622 (1973).
59 C. H. Park, and D. J. Chadi, Phys. Rev. Lett. **76**, 2314 (1996).
60 S. Bhattacharya, R. Basu, R. Bhatt, S. Pitale, A. Singh, D. K. Aswal, S. K. Gupta, M. Navaneethan, and Y. Hayakawa, J. Mater. Chem. A **1**, 11289 (2013).
61 Y. Xia, V. Ozoliņš, and C. Wolverton, Phys. Rev. Lett. **125**, 085901 (2020).
62 G. C. Tewari, T. S. Tripathi, and A. K. Rastogi, J. Elec. Mater. **39**, 1133 (2010).
63 T. R. Wei, Y. Qin, T. Deng, Q. Song, B. Jiang, R. Liu, P. Qiu, X. Shi, and L. Chen, Sci. China Mater. **62**, 8 (2019).